The Astrophysical Journal, 953:150 (10pp), 2023 August 20 https://doi.org/10.3847/1538-4357/ace420
© 2023. The Author(s). Published by the American Astronomical Society.
OPEN ACCESS

Understanding the Deflection of the "Cartwheel CME": Data Analysis and Modeling

Abril Sahade[1,2,3], Angelos Vourlidas[4], Laura A. Balmaceda[5,6], and Mariana Cécere[1,3]
[1] Instituto de Astronomía Teórica y Experimental, CONICET-UNC, Córdoba, Argentina; asahade@unc.edu.ar
[2] Facultad de Matemática, Astronomía, Física y Computación, Universidad Nacional de Córdoba (UNC), Córdoba, Argentina
[3] Observatorio Astronómico de Córdoba, UNC, Córdoba, Argentina
[4] The Johns Hopkins University Applied Physics Laboratory, Laurel, MD 20723, USA
[5] Heliophysics Science Division, NASA Goddard Space Flight Center, Greenbelt, MD 20771, USA
[6] George Mason University, Fairfax, VA 22030, USA
Received 2023 February 15; revised 2023 June 30; accepted 2023 July 2; published 2023 August 14

Abstract

We study the low corona evolution of the "Cartwheel" coronal mass ejection (CME; 2008 April 9) by reconstructing its three-dimensional path and modeling it with magnetohydrodynamic simulations. This event exhibited a double deflection that has been reported and analyzed in previous works but whose underlying cause remained unclear. The Cartwheel CME traveled toward a coronal hole (CH) and against the magnetic gradients. Using a high-cadence, full-trajectory reconstruction, we accurately determine the location of the magnetic flux rope (MFR) and, consequently, the magnetic environment in which it is immersed. We find a pseudostreamer (PS) structure whose null point may be responsible for the complex evolution of the MFR at the initial phase. From the preeruptive magnetic field reconstruction, we estimate the dynamic forces acting on the MFR and provide a new physical insight into the motion exhibited by the 2008 April 9 event. By setting up a similar magnetic configuration in a 2.5D numerical simulation we are able to reproduce the observed behavior, confirming the importance of the PS null point. We find that the magnetic forces directed toward the null point cause the first deflection, directing the MFR toward the CH. Later, the magnetic pressure gradient of the CH produces the reversal motion of the MFR.

Unified Astronomy Thesaurus concepts: Solar prominences (1519); Solar magnetic fields (1503); Solar coronal mass ejections (310); Magnetohydrodynamical simulations (1966)

Supporting material: animation

1. Introduction

Coronal mass ejections (CMEs) are the drivers of the strongest geomagnetic storms and a major concern of space weather. They are usually related to the ejection of magnetic flux rope (MFR) that connects them to the eruptive source region in the lower corona, including prominence/filament eruptions, flares, and cavities (e.g., Zhang et al. 2001; van Driel-Gesztelyi & Green 2015; Green et al. 2018; Jiang et al. 2018; Yang et al. 2018; Filippov 2019). Predicting the occurrence and trajectory of the eruption is crucial for assessing their potential geoeffectiveness. Since the launch of the Solar TErrestrial RElations Observatory (STEREO; Kaiser et al. 2008) twin spacecraft (STA and STB, hereafter), along with the development of various reconstruction tools (e.g., Mierla et al. 2008; Maloney et al. 2009; Temmer et al. 2009; Thernisien et al. 2009; Kwon et al. 2014; Isavnin 2016; Zhang 2021), multipoint observations allow the determination of the three-dimensional (3D) path of CMEs and their associated source regions.

Several factors can deflect an eruption from its radial course (MacQueen et al. 1986; Cremades & Bothmer 2004; Gui et al. 2011; Kay et al. 2015; Sieyra et al. 2020). It is generally accepted that neighboring magnetic structures, such as coronal holes (CHs; e.g., Cremades et al. 2006; Gopalswamy et al. 2009; Sahade et al. 2020, 2021) and active regions (ARs; e.g., Kay et al. 2015; Möstl et al. 2015; Wang et al. 2015), can deflect MFRs in longitude and latitude against their position. On the other hand, heliospheric current sheets (e.g., Liewer et al. 2015; Wang et al. 2020), helmet streamers (e.g., Zuccarello et al. 2012; Yang et al. 2018), and pseudostreamers (PSs; e.g., Cécere et al. 2020; Wang et al. 2020; Karna et al. 2021; Sahade et al. 2022) attract MFRs toward their low magnetic field regions. These responses can be quantified, in strength and direction, by the local and global gradients of the magnetic pressure (Gui et al. 2011; Panasenco et al. 2013; Liewer et al. 2015; Sieyra et al. 2020).

However, there are events that seem to propagate against those gradients, such as the one known as the "Cartwheel CME." This event erupted on 2008 April 9, after 8:45 UT, and has been studied extensively from different perspectives (Landi et al. 2010; Savage et al. 2010; Gui et al. 2011; Patsourakos & Vourlidas 2011; Kliem et al. 2012; Thompson et al. 2012; Capannolo et al. 2017). The eruption followed a nonradial trajectory, according to 3D reconstructions (Landi et al. 2010; Gui et al. 2011; Patsourakos & Vourlidas 2011; Thompson et al. 2012). Landi et al. (2010) first reconstructed the 3D CME core trajectory at eight different times from 1.1–5.1 $R_\odot$ noting that the Cartwheel CME had an initial deviation toward Earth and later it moved away from the direction of Earth. Savage et al. (2010) tracked the erupted material in STA plane-of-sky (POS) with better cadence but in a 2D projection below 1.5 $R_\odot$. They investigated the magnetic field configuration noting that the CME seems to initially move toward the southern open field lines. Later, the trajectory projected in the POS becomes more radial near $\sim$2.5 $R_\odot$. To understand the nonradial evolution of this event, Capannolo et al. (2017) modeled the MFR eruption with ForeCAT (Kay et al. 2013, 2015) and

Original content from this work may be used under the terms of the Creative Commons Attribution 4.0 licence. Any further distribution of this work must maintain attribution to the author(s) and the title of the work, journal citation and DOI.

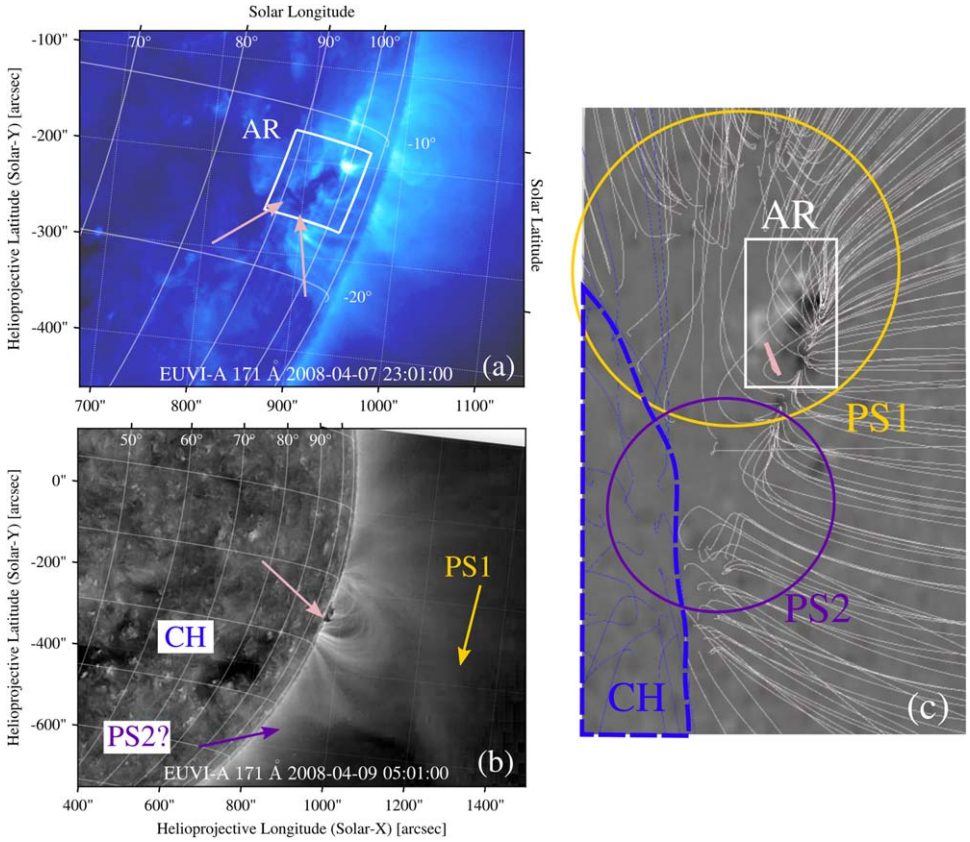

Figure 1. (a) Source region and preeruptive filament (pink arrows) seen by STA on 2008 April 7. The white square indicates the AR as in the right panel. (b) Preeruptive filament (pink arrow) seen by STA on 2008 April 9 hours before the eruption, PS1 is located behind the limb (orange arrow), the CH is seen as a dark patch, and some field lines of PS2 (violet arrow) are possibly seen at the limb. (c) Radial magnetic field B_r at 1 $R_\odot$ in gray scale, open (blue) and closed (white) field lines, the position of the preeruptive filament (pink line) and the magnetic structures surrounding the source region. The white square indicates AR 10989, the pseudostreamers are indicated by circles (in orange PS1, in violet PS2), and the southern CH is delimited by blue dashed lines.

compared it to the reconstructed trajectory of Landi et al. (2010). ForeCAT calculates the deflection and rotation of the simulated MFR (varying initial mass, speed, size, shape, and location) considering the magnetic forces (tension and pressure gradient) from the solar background. Although they were able to reproduce the double deflection, they found that the MFR moved unexpectedly against the magnetic gradients, toward a CH. They needed to assume a nonradial initial velocity to impulse the MFR in this direction and proposed that an asymmetrical reconnection of the footpoints could explain it.

In this paper, we investigate the validity of previous interpretations of the deflection of the Cartwheel CME and find that the eruption is not unusual but follows the expected trajectory along existing magnetic fields. A detailed reconstruction allows us to properly investigate the magnetic interaction between the environment and the Cartwheel CME and provide new insight into the MFR behavior. In Section 2, we reconstruct the 3D path of the 2008 April 9 event with a higher cadence and using different techniques at the low corona. We reconstruct the surrounding magnetic field with the potential field source surface model (PFSS; Schrijver & De Rosa 2003). In Section 3, we present the results of a magnetohydrodynamic (MHD) numerical simulation where an MFR interacts with the main magnetic structure found by the PFSS reconstruction. The simulated event reproduces the Cartwheel CME behavior and allows us to compute the forces acting on the MFR. Conclusions and final comments are presented in Section 4.

2. Data Analysis

2.1. Source Region

Much of the eruptive material belonged to a prominence located within AR 10989. Figure 1 shows the source region in 171 Å from the STA perspective and the magnetic structures near it. Figure 1(a) shows the preeruptive filaments on 2008 April 7, when the AR was still on disk. The eruptive filament was not the one lying along the polarity inversion line in the center of the AR, but the one in the outer part of it (pink arrows). Figure 1(b) shows also the preeruptive filament (pink arrow), the position of a pseudostreamer that overlaid the AR (PS1, orange arrow), the position of the southern CH (blue label), and indicates some lines visible on the limb that may belong to a second pseudostreamer (PS2, violet arrow), all on 2008 April 9 a few hours before the eruption. Figure 1(c) shows the radial magnetic field B_r at 1 $R_\odot$ in gray scale, the open (blue) and closed (white) field lines over it, the position of the preeruptive filament (pink line) of panel (a), and the mentioned magnetic structures surrounding the source region. The white square indicates the AR 10989, the PSs are indicated by circles (in orange PS1, in violet PS2), and the southern CH is delimited by blue dashed lines. The prominence was enclosed by a PS with anemone-like topology (e.g., Mason & Uritsky 2022, PS1, see Figure 1), whose southern side was overlaid by the negative open field of a CH (see Figure 1(c)) and the northern side was overlaid by the negative footpoints of closed field lines. The region was complex and presented more

PS structures, such as PS2 (see Figure 1(c)). The PS topology consists of a separatrix dome above a minority polarity region, and an outer spine emanating from a null point on this dome and connected out into the open heliosphere or to some far distant closed-field region. This is the well-known embedded-bipole topology surrounded by unipolar fluxes of both open or closed (at larger scales) magnetic fields (e.g., Raouafi et al. 2016; Mason et al. 2021; Wyper et al. 2021).

Between 2008 March 22 and 30, the AR exhibited eruptive activity, with a major CME on 2008 March 25. After that, the region remained quiet until 2008 April 3, when it exhibited brightening in the EUV 195 channel and two small eruptions on 2008 April 5. The Cartwheel CME is the last and most notable of the eruptions from this region.

2.2. Prominence and Coronal Mass Ejection 3D Reconstruction

The 2008 April 9 event was observed on the west limb by the Solar and Heliospheric Observatory (SOHO; Domingo et al. 1995) and STEREO spacecraft. At that time, the STEREO spacecraft were separated by ∼24° from Earth. We use the data provided by the Extreme-ultraviolet Imaging Telescope (SOHO/EIT, Delaboudinière et al. 1995), the Large Angle and Spectrometric Coronagraph Experiment (SOHO/LASCO, Brueckner et al. 1995), the wavelet-enhanced images from Extreme-Ultraviolet Imager (STEREO/EUVI, Howard et al. 2008), and COR1 coronagraphs from STEREO spacecraft to reconstruct the trajectory of the prominence and CME. We use Michelson Doppler Imager (SOHO/MDI, Scherrer et al. 1995) data for the days before 2008 April 9 and apply the PFSS model to reconstruct the magnetic field over the solar surface.

Since the source region was located near the western limb of STEREO-A (STA), we reconstruct the initial 3D trajectory from SOHO/EIT and STA/EUVI 195 Å channels. When the prominence appears in the STEREO-B field-of-view (FOV), we track the ejected material in the 171, 195, and 304 Å channels, from both STEREO spacecraft to ensure we are following the same features and cover the broader time range with high cadence. Finally, we track the prominence in white-light images from STEREO/COR1 while it is bright and compact. The 3D location of the prominence is determined using the tie-pointing technique, which consists of a geometrical reconstruction by considering the position of the same feature in the FOV of two different spacecraft (see, e.g., Inhester 2006). We use the `scc _meassure` routine, developed by B. T. Thompson, from SolarSoft. Figure 2 shows the eruption at 09:56 UT from STA and STB perspectives in the different filters. For the 171 and 195 Å filters, we follow the apex of the cold material prominence. In the 304 Å filter and COR1 images, we track the main axis of the prominence, measuring multiple positions each time. The median latitudes and longitudes correspond to the position of the apex. The color-coded dots in Figure 2 summarize the reconstructed trajectory of the prominence apex at each time. Figure 2(b) also indicates the prominence position (pink arrow) and CME front (white dashed lines) at that time.

In addition, we reconstruct the CME from the EUV 195 Å and white-light images from the three viewpoints (SOHO, STA, and STB). To reproduce the evolution of the deflecting CME from the low corona we use, for the first time, a nonradial graduated cylindrical shell (GCS) model. In this way, the CME footpoint coordinates can be fixed while the CME front can vary in latitude and longitude. We use the SolarSoft routine `rtcloudwidget`, the parameters tuned for the reconstruction are latitude, longitude, tilt angle, height, half angle, ratio, and nonradial tilt. The latter allows to change the angle subtended by the CME axis and the radial plane defined by the footpoints and the solar center. This adds a degree of freedom in the reconstruction, which may produce a new set of solutions. However, as the footpoints are characterized by the latitude, longitude, and tilt angle these parameters remain unchanged throughout the full evolution of the CME. This is an improvement over previous reconstructions as the deflection can be better captured and the coordinates of the CME front are more accurately determined while CME footpoints remain in the source region. Figure 3 shows the projected centers of the CME modeled by the GCS in color dots (from 9:25 UT in violet to 11:45 UT in yellow), left panels show the base difference images of 195 Å filters (for STA, SOHO, and STB) and the GCS wire and cross-section circle for 10:05 UT, right panels show the base difference of white-light images (also for STA, SOHO, and STB) including the projected cross-section circles of the GCS model. Table 1 shows the parameters used for the nonradial GCS reconstruction and Table 2 (Appendix) shows the coordinates for both GCS and triangulation reconstruction techniques, for the prominence and the CME, in EUV and white-light images, respectively. The prominence is tracked from 08:15–11:15 UT (1.03–3.08 $R_\odot$), and the CME can be modeled from 09:25–11:45 UT (1.24–4.1 $R_\odot$).

Figure 4 shows the triangulated prominence trajectory and the surrounding PFSS magnetic field lines. Again, the main magnetic structures near the source region are indicated (PS1, orange circle; PS2, violet circle, AR, white square, CH, blue lines). The prominence initially departed from a complex region of closed loops (white lines) at Carrington longitude and latitude (195°, −16°). It traveled toward the open magnetic field of a southern CH (blue lines) until reaching (182°, −29°). Afterward, the prominence changed its motion and traveled outward along the open magnetic field lines, with coordinates (196°, −26°) in the last measured position. The purple line marks the radial direction from the initial position of the eruptive material, with ticks from 1.2–2.8 $R_\odot$. The prominence apex changed in both latitude and longitude, but it is possible to define a plane intersecting the solar sphere, which contains the evolution of the apex (hereafter, the plane of eruption (POE)). The POE is selected by nonlinear least-square fitting and presents a standard deviation lower than 1°, indicating that the apex moved within a plane (light blue plane of Figure 4). Figure 4(b) shows a rotated view of the eruption in which the POE is parallel to the POS and the radial direction is pointing upwards. We define a Cartesian reference system with the x-axis being parallel to the solar surface at the initial position of the prominence, the y-axis pointing in the radial direction, and z-axis perpendicular to the POE. In this system, the outward motion is projected in the y-direction and the deflections in the x-direction. For reference, the solar equator is shown in teal color. Figure 4(c) shows a closer view of the source region and the initial triangulated position of the prominence. It includes the radial magnetic field at 1 $R_\odot$ and the isocontours of magnetic field strength to show the 3D location of null points. Null points are located in the purple contours. In particular, we notice the one corresponding to PS1 (orange circle) and PS2 (violet circle). From this view, we see how the projection of the POE (pink line) crosses the different structures, such as the

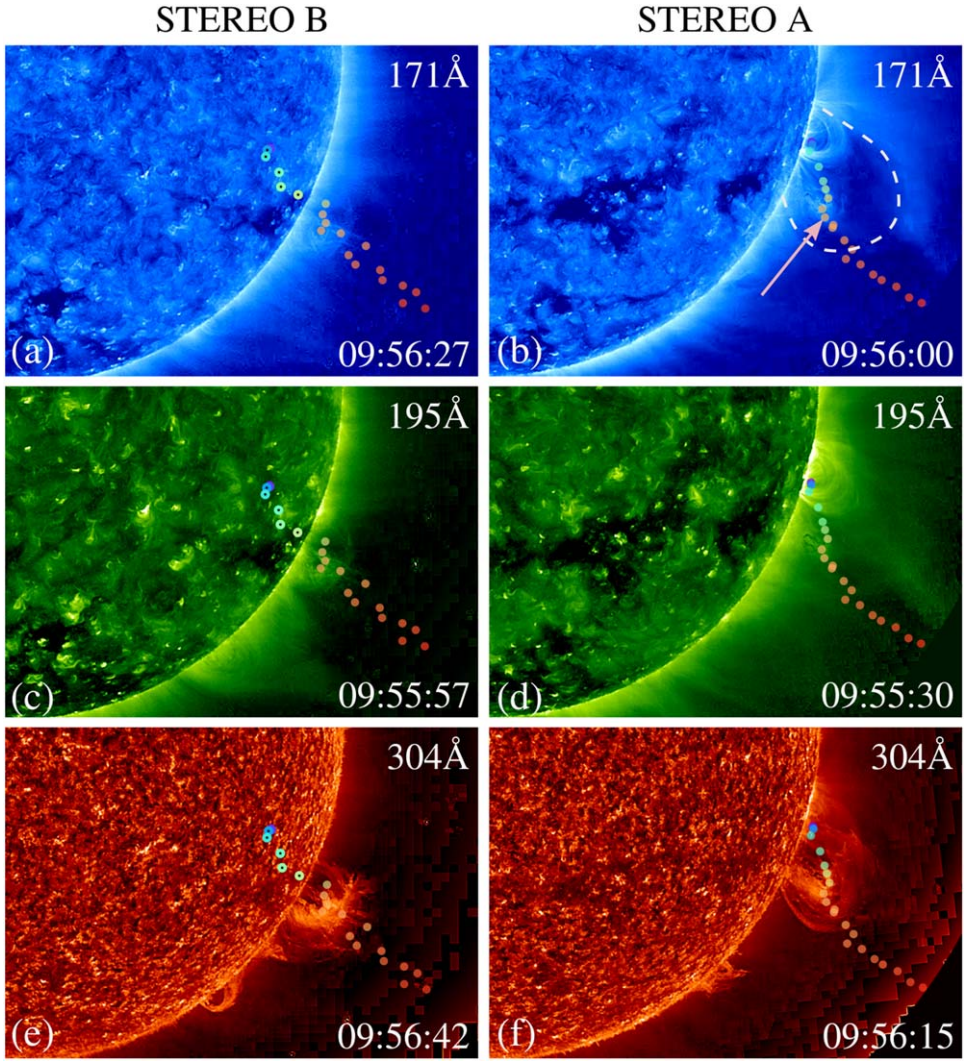

Figure 2. 2008 April 9 event in STEREO 171, 195, and 304 Å filters at 09:56 UT. Rainbow-colored dots represent the apex position of the prominence from 8:25 UT (violet dot) to 10:40 UT (red dot), triangulated in EUVI images. The left panels show STB FOV, dots with the black center are behind the limb and are triangulated with SOHO/EIT; the right panels show STA FOV. Panel (b) indicates also the prominence position with the pink arrow, and the CME front in white dashed lines.

external border of the AR, a lobe of PS1, PS2, and the CH. The preeruptive filament is drawn in light pink is drawn.

By defining the POE we can study the magnetic scenario that produces the nonradial motion in a simpler way as we reduce the dimension of the problem. We assume that the forces along the third dimension of this projection (z-axis) are balanced because the system did not suffer displacements in that direction. Figure 5 shows the magnetic field magnitude in logarithmic scale, the magnetic field lines and the prominence position (rainbow dots, obtained by triangulation), the CME center position (magma dots with gray edges, obtained from the nonradial GCS model), and the CME cross section (gray circles, obtained from the nonradial GCS model) projected on the POE, in the Cartesian reference system described above. The PS located at $x \sim 0.2\,R_\odot$ is PS2. To the left of PS2, there are the closed field lines belonging to the helmet streamer that encloses PS1, the orange magnetic field intensity at $x \sim -0.2\,R_\odot$ belongs to the outer part of the AR. To the right of PS2, there are the open field lines of the CH. From the early reconstruction of the prominence path, we can see that it headed toward the null point (gray star) of PS2 located at $(x,\ y) = (0.16\,R_\odot,\ 1.05\,R_\odot)$, then both the CME and the prominence moved to the right (in this coordinate system) displacing $\sim 15°$ from the radial direction. About $1.8\,R_\odot$ they reversed the motion traveling to the left and aligning with the CH field lines. The final angle of deflection is lower than 5°. This double-deflection behavior was previously reported in Sahade et al. (2021). Their scenario did not include a PS configuration as in the case here, but the interaction with the PS null point and the open magnetic field lines is quite similar (see Section 3 for further analysis). It is interesting to note the evolution of the prominence relative to the CME. Initially, the prominence was located close to the right edge of the MFR cross section, exhibiting a larger deflection than the MFR center (the maximum being 18° and 14°, respectively). In the later stages, the prominence apex progressively reached the MFR center, in both displacement x and height y. This behavior appears consistent with the prominence material lying at the bottom of the MFR due to the gravity and the balance of magnetic forces (e.g., Vourlidas et al. 2013). As the MFR moved nonradially, the prominence followed along the edge of the cavity, experiencing larger deflection possibly because of its larger inertia. The displacement between the MFR and the prominence is noted in the STA images (see Figure 2(b), where

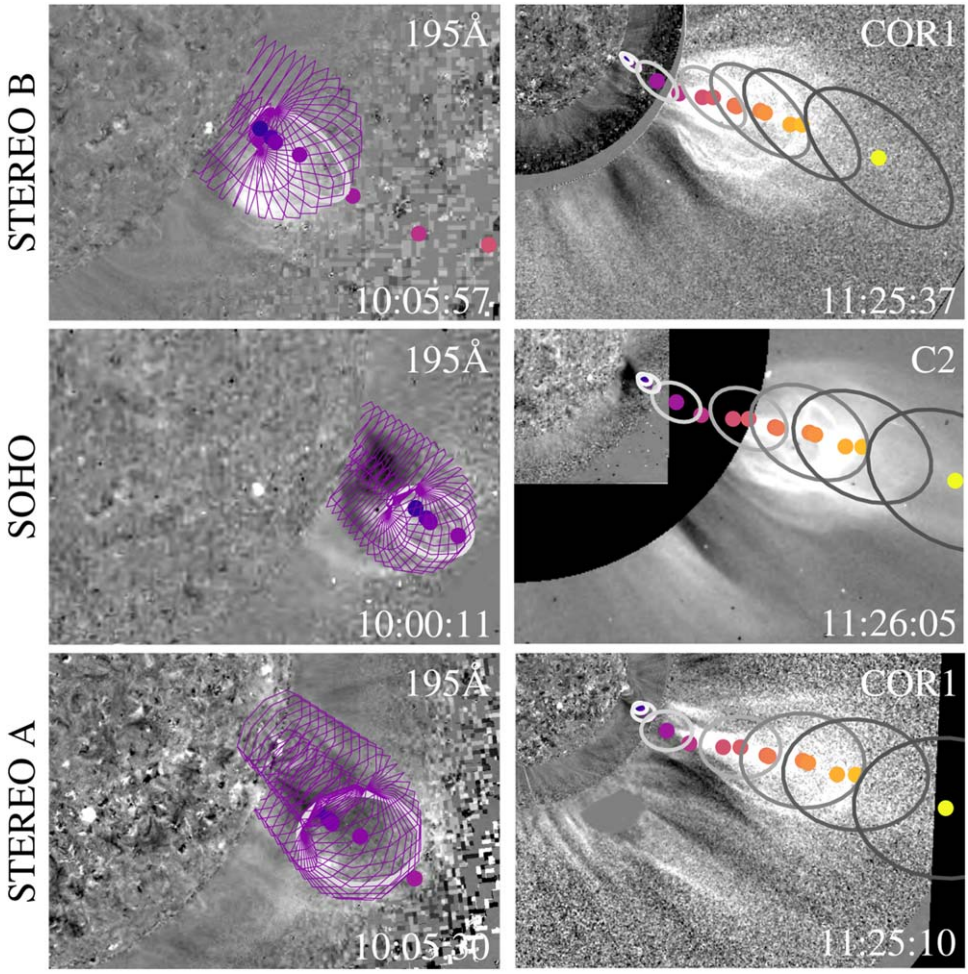

Figure 3. 2008 April 9 event in STA, SOHO, and STB in the 195 Å filter (left) and coronagraph (right) images. Images are processed with base difference. Color dots represent the position of the CME center from 9:25 UT (violet dot) to 11:45 UT (yellow dot). The GCS reconstruction at 10:05 UT (magenta wire frame) and its central cross section (white circle) is plotted over the 195 images. The cross sections (gray circles) of the GCS reconstruction and centers (color dots) from 9:25–11:45 UT are overplotted on the coronagraph composites in the right panels.

the position of the prominence was not centered with the CME front) but 3D measurements give us certainty that the actual trajectories differ and that it is not a projection effect. It may be due to changes in the MFR shape (i.e., contraction) as the prominence material expanded and/or drained out. It is difficult to reach robust conclusions without detailed information on the prominence of physical properties as it evolves, which is unavailable.

2.3. Magnetic Forces

The PFSS model is useful for understanding the global magnetic environment and large-scale structures surrounding the eruptive material. However, it cannot account for the magnetic field evolution during an eruption unless the eruption produces photospheric changes, which is observed only in large eruptions. From this reconstruction technique, we recover a PS null point which may be *attracting* the MFR and directing it toward the open magnetic field lines of the nearby CH. Figure 6 shows the temporal evolution of the angular alignment between the MFR trajectory and both the magnetic field lines (B-T orange line) and the gradient of magnetic pressure (with the conventional minus sign in front, i.e., $\boldsymbol{G} = -\nabla\frac{B^2}{2\mu_0}$; G-T teal line). In the initial phase of the eruption (8:45–9:35 UT; below 1.2 $R_\odot$), the MFR moved slightly misaligned with the gradient direction, but since the MFR did not stop in the PS2 null point the misalignment grows to 100°. In the second phase (until 10:35 UT and 1.8 $R_\odot$), the MFR moved along the CH magnetic field lines, aligning with both the gradient and field as it lost speed in the x-direction. In the third phase of the evolution, the misalignment remains small but with an increasing trend. This can be understood as the dynamical response of the CH, which was compressed by the inertial motion of the MFR and later returned the MFR to the original position of the open field lines. At 11:00 UT, and above 2.5 $R_\odot$, the CME stopped the x displacement, confined in the lines of the CH.

To estimate the force exerted by the CH on the MFR, we consider flux conservation of the CH magnetic field lines. Without magnetic reconnection, the field lines should be pushed inward, reducing the CH area and proportionally increasing its magnetic field strength in the B_y component. Considering this, we estimate the magnetic pressure gradient in the x-direction. We also obtain a polynomial fitting for the trajectory, and derive the radial (y-direction) and nonradial (x-direction) velocity and acceleration. Figure 7 compares the normalized magnitude of the force produced by the magnetic pressure gradient and the normalized magnitude of the MFR acceleration in the x-direction. In this evolution period the

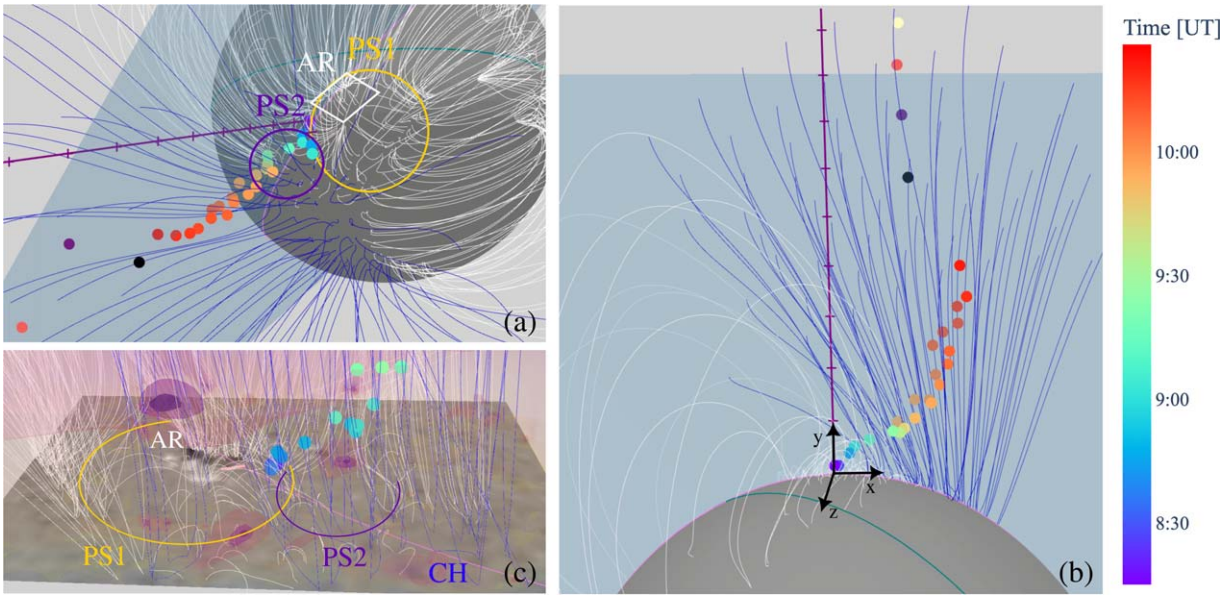

Figure 4. (a) Triangulated trajectory of the prominence apex with the PFSS magnetic field lines. White magnetic field lines are closed and blue ones are open lines of positive polarity. Rainbow-colored dots show the prominence triangulation in EUVI images. Black, violet, pink, and beige dots are triangulated in COR1 images at 10:45, 10:55, 11:05, and 11:15 UT, respectively. In purple, the radial direction according to the initial position of the prominence, with markers separated by 0.2 $R_\odot$. In light blue, the plane where the trajectory lies, the pink circle shows the intersection of this POE and solar surface, the teal circle represents the equator. Magnetic structures PS1, PS2, AR, and CH idem Figure 1. (b) Rotated position of the eruption and magnetic field lines. Cartesian axes defined from the POE. (c) Radial magnetic field B_r at 1 $R_\odot$ in gray scale with isocontours of magnetic field strength in purple shades. The spots of stronger purple show the 3D location of the minimum magnetic field. The magnetic field lines are plotted in blue (open) and white (closed), also the position of the preeruptive filament (light pink line), and the pink circle showing the POE projection over the surface of the plane. The magnetic structures are the same as in panel (a).

Table 1
Nonradial GCS Parameters

Time (UT)	Height ($R_\odot$)	Aspect Ratio	Nonradial Tilt (°)
09:25	1.34	0.05	−33.5
09:35	1.35	0.06	−34.2
09:45	1.42	0.08	−34.2
09:48	1.43	0.08	−34.2
10:00	1.46	0.09	−34.8
10:05	1.56	0.12	−29.8
10:14	1.84	0.14	−29.8
10:26	2.11	0.14	−25.5
10:40	2.38	0.14	−15.5
10:45	2.57	0.16	−11.2
10:55	2.92	0.19	−9.3
11:05	3.30	0.20	−5.6
11:10	3.37	0.20	−5.6
11:20	3.70	0.20	−5.6
11:25	3.88	0.20	−3.7
11:45	4.91	0.20	−3.7

Note. Height parameter corresponds to the CME front height, the aspect ratio indicates the relation between height and the cross section of the CME, and the nonradial tilt gives the angle between the radial direction and the CME axis. The other parameters of the model remain fixed: latitude $\theta = -17°$, longitude $\phi = 196°$, tilt $\gamma = -42.5°$, and half angle $\alpha = 4.5°$. Times up to 10:40 UT correspond to EUV images, and times after 10:45 correspond to coronagraph images.

acceleration is directed to the $-x$-direction and increases until $\sim$1.7 $R_\odot$ (10:20 UT), then gradually reduces to zero. Since the trend of both curves is quite similar we suspect that the magnetic pressure gradient is contributing to accelerating the MFR out of the CH during their interaction.

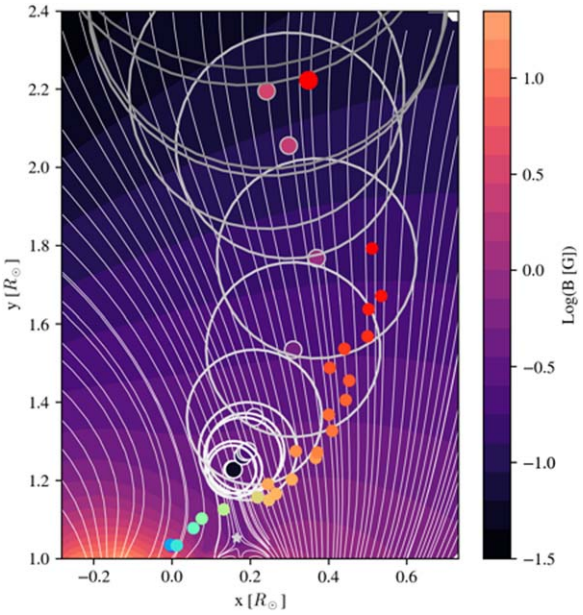

Figure 5. Magnetic field magnitude (logarithmic scale) and field lines with the prominence and CME trajectory in the POE. The gray star indicates the null point position of PS2. Rainbow-colored dots correspond to the triangulated positions of the prominence with the same timescale as Figure 4 and the last larger red dot being the black one used in Figure 4. White to gray circles represent the cross sections of the nonradial GCS model from 9:25–11:20 UT, and color dots with the same white/gray edges represent the centers of each cross section, up to 10:45 UT.

3. Numerical Simulation

In Sahade et al. (2022, hereafter S22) we modeled a MFR immersed in a PS magnetic field and studied the dynamical interaction between both structures while changing the

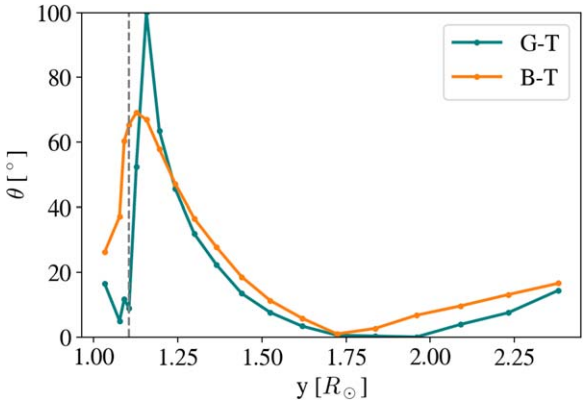

Figure 6. Angle of misalignment between the magnetic gradient and trajectory (G-T), and the magnetic field and trajectory (B-T). The gray dashed line indicates the height at which the PS spine is crossed.

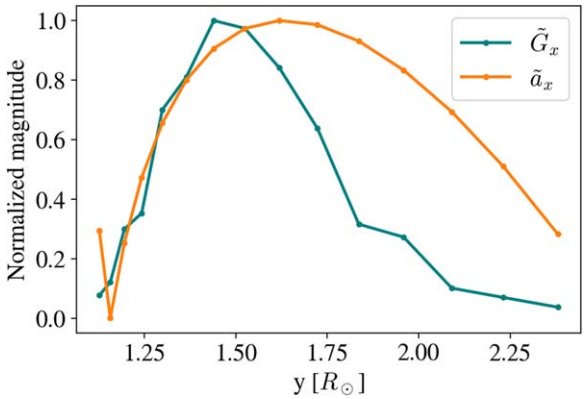

Figure 7. Normalized magnetic gradient pressure ($\tilde{G}_x$) and normalized acceleration ($\tilde{a}_x$) in the x-direction during the observed interaction between the MFR and the CH.

parameters. For this work, we adapt the model used in that work to simulate the magnetic configuration of the 2008 April 9 event. The Cartwheel CME seems to interact with the null point of a nearby small PS (PS2) and then with the CH overlying the southern lobe of that PS. By adjusting the model parameters and modifying Equations 11(a) and (b) of S22 to obtain a bent PS spine, we establish an initial magnetic field configuration that has a topology and magnetic field strength similar to those shown in Figure 5. The new equations for the background magnetic field allow a shift of the central position of the potential magnetic field overlying the PS:

$$B_x(x, y) = \frac{2\sigma B_{\rm PS}(x - x_{\rm PS})(y - y_{\rm PS})}{((x - x_{\rm PS})^2 + (y - y_{\rm PS})^2)^2} + B_0 \sin\left(\frac{x - x_{\rm CH}}{H}\right)\exp[-y/H], \quad (1)$$

$$B_y(x, y) = -\frac{2\sigma B_{\rm PS}(x - x_{\rm PS})^2}{((x - x_{\rm PS})^2 + (y - y_{\rm PS})^2)^2} + \frac{\sigma B_{\rm PS}}{(x - x_{\rm PS})^2 + (y - y_{\rm PS})^2} + B_0 \cos\left(\frac{x - x_{\rm CH}}{H}\right)\exp[-y/H], \quad (2)$$

where $B_{\rm PS} = -0.7$ G is the magnetic field strength due to a single line dipole ($\sigma = 3 \times 10^{19}$ is a dimensionless scaling factor) located at $(x, y) = (x_{\rm PS}, y_{\rm PS})$, where $x_{\rm PS} = 120$ Mm and $y_{\rm PS} = -10$ Mm, $B_0 = 1$ G is the background field strength at $(x, y) = (x_{\rm CH}, 0)$, where $x_{\rm CH} = 200$ Mm, and $H = 400$ Mm is the height decay factor. The rest of the simulation parameters are set as in S22 except for the current densities here being $j_0 = -700$ statA cm^{-2}, $j_1 = 516$ statA cm^{-2}.

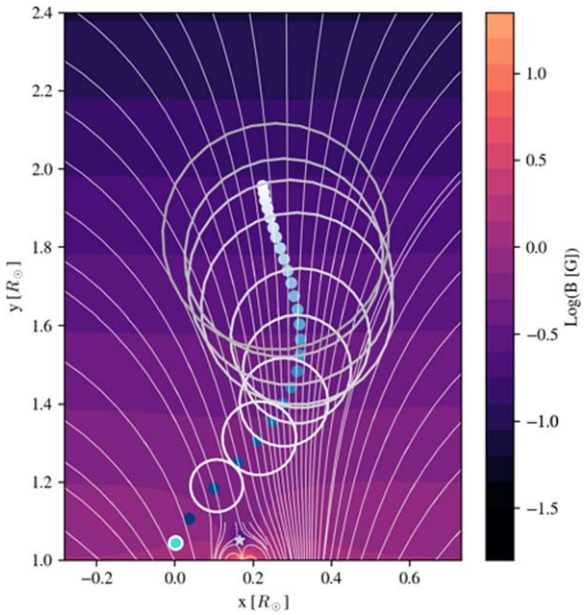

Figure 8. Background magnetic field magnitude and lines of the simulated case. The turquoise dot indicates the initial position of the FR, and the gray star indicates the observed PS null point position. The MFR cross section and center are represented by white/gray-scaled circles and blue-scaled dots, respectively.

Figure 8 shows the background magnetic field resulting from Equations (1) and (2), where the MFR is added. The turquoise dot and the gray star indicate the prominence initial position and PS2 null point position from the observational data, respectively. The null point position, the width of the PS, and the magnetic field strength are well reproduced (compare to Figure 5) by the parameter selection. We note that above $y = 2\,R_\odot$ and beyond $x = 0.4\,R_\odot$, the field lines behave differently than in Figure 5. This is expected since the model assumes a simpler configuration than the actual solar magnetic field. However, it is not necessary to modify the magnetic field configuration to fit those farther regions since our intention is to understand the initial behavior of the MFR. The blue-scaled dots and gray circles show the evolution of the MFR center and cross section, respectively. While the trajectory and the MFR size are comparable, the simulation evolves faster than the observed case.

Figure 9 shows the gas pressure distribution and magnetic field lines of the simulation at $t = 1900$ s. We note the MFR (delimited by the low-pressure cavity) is displaced to the right and expanded compared to its initial position and volume (see the full evolution in the animated version). During its ascent, the MFR develops a super-Alfvénic shock ahead of the cavity. The shock interacts with the CH bending its field lines. In the MFR separatrix, there is a flux cancellation region (bottom-right diagonal of the MFR) that leads to reconnection and magnetic islands formation. In the animated version, we can follow a magnetic island, located at $(x, y) \sim (0.4\,R_\odot, 1.4\,R_\odot)$ at

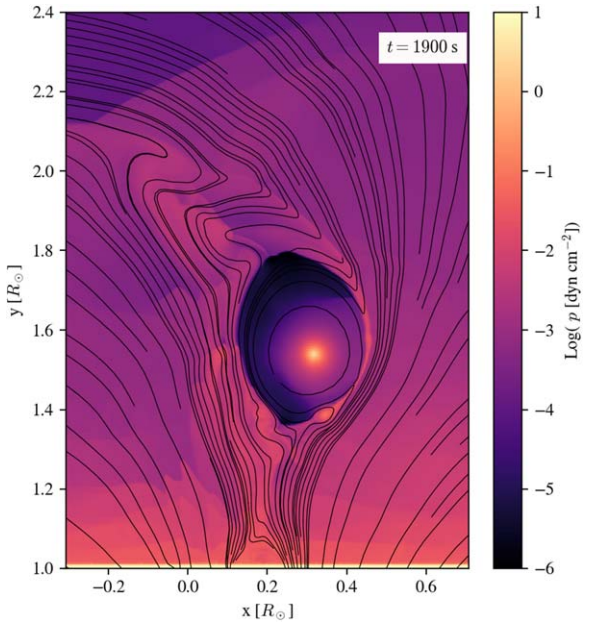

Figure 9. Gas pressure distribution and magnetic field lines at $t = 1900$ s from the numerical simulation. The field line density is higher in the PS and MFR region to better capture the evolution of these structures ($x \sim [0.1–0.3]\ R_\odot$). An animated version of this figure, showing the magnetic field lines and pressure evolution, is available in the HTML version. The animation shows the MFR evolution during the first 3000 s of the simulation, during the first 1900 s the MFR evolves toward the right, pushing and bending the CH magnetic field lines, and later the MFR continues its rise moving back to the left. The gas pressure shows the evolution of plasma features such as the MFR, the shock front, and the magnetic islands around the MFR.

(An animation of this figure is available.)

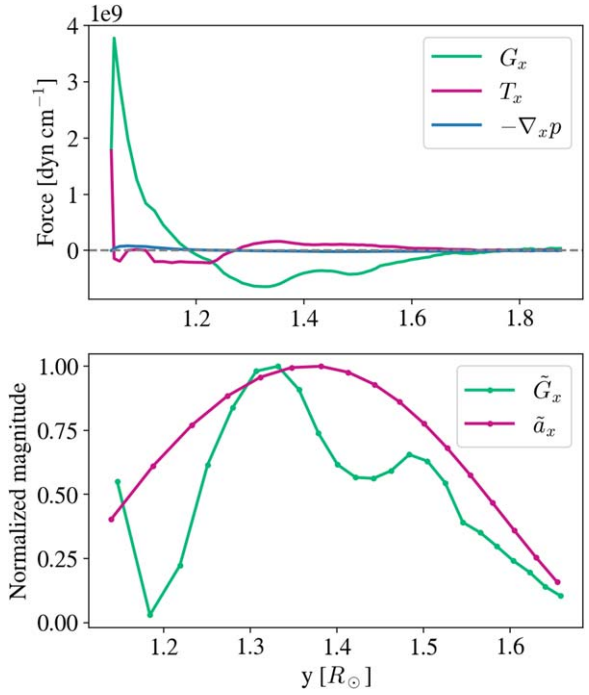

Figure 10. Upper panel: forces per length unit in the x-direction exerted on the MFR. Magnetic pressure gradient (G_x), magnetic tension (T_x), and gas pressure gradient ($-\nabla_x p$) for the first 4000 s of the simulation. Lower panel: normalized magnetic gradient pressure ($\tilde{G}_x$) and normalized fit acceleration ($\tilde{a}_x$) in the x-direction for the simulated MFR during the interaction with the open field lines.

$t = 1500$ s, as it rotates along the MFR edge almost 90° in 900 s, and it is lost within the turbulence afterward.

The simulated scenario reproduces the behavior observed in the Cartwheel CME. The MFR travels toward the null point location and it continues the lateral motion pushing the CH field lines. The CH lines are initially bent by the shock and the MFR, but they eventually stop the rightward motion of the MFR, push back, and guide the MFR back to the original position of the CH lines. From the dynamic evolution of the magnetic field, we can calculate the forces exerted on the MFR during its ascent. Figure 10 shows the evolution of the MFR forces per length unit (since the simulation is 2.5D) in the x-direction in the upper panel. The magnetic forces have a larger contribution than the gas pressure, and both magnetic pressure gradient and tension accelerate the MFR to the right (toward the null point) in the initial phase of the evolution. The magnetic forces are driving the MFR toward the null point position. When the MFR begins to interact with the open magnetic field lines of the CH, the magnetic pressure gradient becomes negative, stopping the rightward motion. The maximum MFR displacement occurs at $y \sim 1.6\,R_\odot$ (and $x \sim 0.3\,R_\odot$ as observed). After that, the negative magnetic pressure gradient increases linearly to zero, as the magnetic tension decreases to zero. Thereafter, the magnetic pressure exerted by the open magnetic field lines restores the MFR to the force-free direction. To compare with Figure 7, the lower panel of Figure 10 shows a zoom-in of the height of the normalized magnetic gradient pressure ($\tilde{G}_x$) and normalized fit acceleration ($\tilde{a}_x$) in the x-direction during the interaction with the open field lines. For the simulation, in agreement with the observational analysis, the acceleration is directed to the $-x$-direction and gradually reduces to zero. Also, the trend of the magnetic gradient is similar to the acceleration, indicating its contribution to the MFR deceleration during the interaction between the MFR and the CH.

4. Discussion and Conclusions

The Cartwheel CME is a well-studied event with a dynamic behavior that appears to run contrary to the current understanding of the interaction between MFRs and ambient magnetic structures (Capannolo et al. 2017). To investigate whether the CME's behavior was indeed unusual, we first focus on obtaining a more precise reconstruction of the event than previous attempts (Landi et al. 2010; Gui et al. 2011; Patsourakos & Vourlidas 2011; Thompson et al. 2012). To achieve this, we use data from three different viewpoints (SOHO, STA, and STB) and two different techniques to reconstruct the evolution of different components of the magnetic system within $4\,R_\odot$. Furthermore, we reconstruct the CME using the nonradial GCS model to better capture the nonradial motion of this event. Our reconstructions are consistent with the assumption that the prominence material is located at the bottom of the MFR. The measurements indicate that the prominence undergoes a larger deflection than the MFR center, due possibly to the higher momentum of the heavier prominence material.

Although the deflection produced changes in both latitude and longitude for the prominence apex and MFR, the entire evolution of them can be projected onto a 2D plane, which simplifies the analysis of the magnetic field configuration in which the MFR moved (see Figures 4 and 5). As established before (Savage et al. 2010; Capannolo et al. 2017), the MFR

was interacting with the open magnetic field lines of a CH, traveling toward them, and against the magnetic gradients. Our thorough reconstruction of the initial rising phase and magnetic field allows the identification of a pseudostreamer (PS2) null point located between the initial position of the MFR and the CH. Considering the action of null points in trajectory (e.g., Panasenco et al. 2013; Wang et al. 2020; Sahade et al. 2021, 2022), we presume that this null point was responsible for attracting the MFR toward the CH, which then stopped the MFR deviation and guided it parallel to its magnetic field lines. Then, the peculiar behavior of the 2008 April 9 CME can be explained not only by assuming an asymmetric magnetic reconnection (Capannolo et al. 2017), but as a response to the interaction with the magnetic environment near the source region.

We analyze the alignment between the trajectory and the magnetic pressure gradient (see Figure 6) and observe different phases in the evolution. Initially, as expected, the angle is small as the MFR traveled toward the null point, then it increases abruptly as the MFR crossed the null point location. Once inside the CH, the MFR trajectory smoothly aligned with both the magnetic gradient and magnetic fields. Finally, we see that the misalignment between the angles increases, presumably because the CH is reacting to the MFR displacement and pushing it back toward a more radial path. In conclusion, our analysis indicates that the MFR tried to align with the magnetic pressure gradient. However, it should be noted that null points can lead to stronger deflections producing misalignment, and also, at later evolution, the angles calculated from the static magnetic field extrapolation may not reflect the responses of the magnetic structure. We estimate the dynamic magnetic pressure gradient exerted by the CH on the MFR (Figure 7) and find that it correlates with the nonradial acceleration of the MFR. Consequently, we conclude that the magnetic pressure gradient is at least one of the restorative forces producing the reversal deflection.

We perform ideal MHD simulations to model the dynamics of the 2008 April 9 event, adapting the magnetic scenario explored in S22. The simulation considers an MFR interacting with a PS structure similar to the observed one (see Figures 8 and 9), other magnetic structures as the nearby AR are excluded from the modeling since they are not contained in the POE. The simulated MFR presents the same double-deflection behavior as the Cartwheel CME, validating the relevance of the null point and magnetic configuration. We calculate the forces acting over the MFR by considering the dynamic evolution of the environment. Initially, the magnetic tension and the magnetic pressure gradient are responsible for deviating the MFR in a nonradial direction and toward the null point. Then, the magnetic pressure gradient is the restoring force that stops the MFR deflection and pushes it back toward a direction more aligned with the original CH lines, agreeing with the data analysis.

In summary, we find, observationally and numerically, that the behavior of the Cartwheel CME can be explained once the trajectory and magnetic environment are well described. The evolution can be divided into three phases. The first one is driven by the presence of the PS2 null point (deflection to the south until 10:09 UT), the second one consists of the response to the CH (reversal deflection), and the third one concerns the MFR outward propagation parallel to the magnetic field lines following the least resistance path (near radial trajectory after 11:05 UT).

The most important conclusions drawn from this work are as follows:

1. The dynamic behavior of the CME was not unusual but rather as expected. The CME escapes through the nearest null point as expected on physical considerations. The apparent *rolling* behavior and sharp direction change were due to the topological configuration in the vicinity of the eruption.
2. Multiviewpoint observations of the low coronal evolution of an eruption are key for understanding the topological environment around the erupting MFR. They can provide essential information to understand unexpected behaviors.
3. Null points play a key role in the early evolution of erupting MFRs. Identifying their presence, and more generally, determining the ambient magnetic topology, will greatly improve our understanding of the early development and trajectory of eruptions.
4. 2.5 MHD numerical simulations provide a useful tool to study different scenarios in which an MFR can evolve. They are computationally less expensive than, for example, data-driven models and allow us to test the interpretations that cannot be easily verified with data.

Recent developments in instrumentation and observations promise great opportunities for further understanding the early evolution of CMEs. EUV and white observations from Solar Orbiter provide a *third* eye to the observations from STEREO, and Earth-based assets (e.g., SDO, GOES/SUVI, and SWFO-L1 in 2025+) from widely variable viewpoints. The future addition of off Sun-Earth line magnetograms (via ESA's Vigil mission, currently in development) will further enhance the reliability of magnetic field extrapolations and consequently of topological maps of the solar corona.

Acknowledgments

We thank the referee for useful comments that have improved the manuscript. A.S. is a doctoral fellow of CONICET. A.S., A.V., and L.A.B. are supported by NASA grant No. 80NSSC19K0069. M.C. is member of the Carrera del Investigador Científico (CONICET). A.S. and M.C. acknowledge support from SECYT-UNC grant PC No. 33620180101147CB, and support from PIP under grant No. 11220200103150CO. We also thank the Centro de Cómputo de Alto Desempeño (UNC), where the simulations were carried out. The work presented here was carried out at JHU/APL and GMU as part of a research internship. A.S. thanks JHU/APL and GMU for their hospitality.

Appendix
Prominence and CME 3D Reconstruction

Table 2 displays the 3D coordinates for each timestamp with the different techniques, instruments, and features of the erupting structure.

Table 2
Spherical Coordinates of the Prominence Apex, CME Center, and CME Apex

Time (UT)	Prominence Apex			CME Center				CME Apex		
	R ($R_\odot$)	θ (°)	ϕ (°)	R ($R_\odot$)	θ (°)	ϕ (°)		R ($R_\odot$)	θ (°)	ϕ (°)
08:15	1.03*	−16.2	195.4				…			
08:25	1.03*	−16.4	195.4				…			
08:45	1.03*	−16.6	196.2				…			
09:15	1.08*	−19.7	194.7				…			
09:25	1.11*	−21.6	195.1	1.24	−22.1	188.4		1.29	−23.0	187.5
09:35	1.13*	−22.3	191.8	1.24	−22.2	188.3		1.30	−23.3	187.2
09:45	1.18*	−22.9	186.5	1.27	−22.8	187.6		1.36	−24.1	186.2
09:48	1.18	−22.9	186.5	1.29	−23.0	187.4		1.38	−24.3	186.0
09:51	1.18	−24.6	186.0				…			
09:53	1.19	−25.5	185.9				…			
09:56	1.24	−26.1	184.4				…			
09:58	1.21	−26.3	188.4				…			
10:01	1.31	−27.8	181.8	1.29	−23.2	187.3		1.40	−24.8	185.5
10:03	1.31	−28.9	186.4				…			
10:06	1.32	−28.2	184.0	1.38	−23.3	187.1		1.54	−24.9	185.3
10:08	1.39	−28.8	182.2				…			
10:09	1.43	−28.5	183.9				…			
10:11	1.47	−28.3	181.8				…			
10:13	1.52	−28.3	182.0	1.56	−25.1	185.1		1.78	−26.7	183.3
10:16	1.54	−29.3	186.1				…			
10:18	1.60	−28.9	184.4				…			
10:09	1.64	−29.6	182.6				…			
10:21	1.71	−29.4	183.3				…			
10:23	1.75	−29.0	181.9				…			
10:26	1.86	−27.3	183.1	1.81	−25.4	184.8		2.05	−26.6	183.4
10:40		…		2.08	−22.9	187.6		2.36	−23.5	186.9
10:45	2.25	−26.3	192.4	2.21	−21.5	189.0		2.56	−22.0	188.5
10:55	2.47	−22.8	191.3	2.45	−21.0	189.5		2.91	−21.5	189.1
11:05	2.80	−25.2	194.5	2.76	−19.6	190.9		3.30	−21.5	190.7
11:15	3.08	−26.2	195.7	2.81	−19.6	190.9		3.36	−19.9	190.7
11:20		…		3.09	−19.8	190.8		3.70	−20.0	190.6
11:25		…		3.24	−18.9	191.7		3.87	−19.0	191.5
11:45		…		4.10	−19.1	191.5		4.91	−19.2	191.4

Note. The coordinates of the prominence apex are determined with the tie-pointing technique, using STA and STB spacecraft (* use STA and SOHO). The coordinates of the CME (center and apex) are determined from the nonradial GCS reconstruction, using STA, STB, and SOHO images. Times until 10:40 UT correspond to EUV images, and times from 10:45 correspond to coronagraph images.

ORCID iDs

Abril Sahade https://orcid.org/0000-0001-5400-2800
Angelos Vourlidas https://orcid.org/0000-0002-8164-5948
Laura A. Balmaceda https://orcid.org/0000-0003-1162-5498
Mariana Cécere https://orcid.org/0000-0002-9844-0033

References

Brueckner, G. E., Howard, R. A., Koomen, M. J., et al. 1995, SoPh, 162, 357
Capannolo, L., Opher, M., Kay, C., & Landi, E. 2017, ApJ, 839, 37
Cécere, M., Sieyra, M. V., Cremades, H., et al. 2020, AdSpR, 65, 1654
Cremades, H., & Bothmer, V. 2004, A&A, 422, 307
Cremades, H., Bothmer, V., & Tripathi, D. 2006, AdSpR, 38, 461
Delaboudinière, J. P., Artzner, G. E., Brunaud, J., et al. 1995, SoPh, 162, 291
Domingo, V., Fleck, B., & Poland, A. I. 1995, SoPh, 162, 1
Filippov, B. P. 2019, PhyU, 62, 847
Gopalswamy, N., Mäkelä, P., Xie, H., Akiyama, S., & Yashiro, S. 2009, JGRA, 114, A00A22
Green, L. M., Török, T., Vršnak, B., Manchester, W., & Veronig, A. 2018, SSRv, 214, 46
Gui, B., Shen, C., Wang, Y., et al. 2011, SoPh, 271, 111
Howard, R. A., Moses, J. D., Vourlidas, A., et al. 2008, SSRv, 136, 67
Inhester, B. 2006, arXiv:astro-ph/0612649
Isavnin, A. 2016, ApJ, 833, 267
Jiang, C., Feng, X., & Hu, Q. 2018, ApJ, 866, 96
Kaiser, M. L., Kucera, T. A., Davila, J. M., et al. 2008, SSRv, 136, 5
Karna, N., Savcheva, A., Gibson, S., et al. 2021, ApJ, 913, 47
Kay, C., Opher, M., & Evans, R. M. 2013, ApJ, 775, 5
Kay, C., Opher, M., & Evans, R. M. 2015, ApJ, 805, 168
Kliem, B., Török, T., & Thompson, W. T. 2012, SoPh, 281, 137
Kwon, R.-Y., Zhang, J., & Olmedo, O. 2014, ApJ, 794, 148
Landi, E., Raymond, J. C., Miralles, M. P., & Hara, H. 2010, ApJ, 711, 75
Liewer, P., Panasenco, O., Vourlidas, A., & Colaninno, R. 2015, SoPh, 290, 3343
MacQueen, R. M., Hundhausen, A. J., & Conover, C. W. 1986, JGR, 91, 31
Maloney, S. A., Gallagher, P. T., & McAteer, R. T. J. 2009, SoPh, 256, 149
Mason, E. I., Antiochos, S. K., & Vourlidas, A. 2021, ApJL, 914, L8
Mason, E. I., & Uritsky, V. M. 2022, ApJL, 937, L19
Mierla, M., Davila, J., Thompson, W., et al. 2008, SoPh, 252, 385
Möstl, C., Rollett, T., Frahm, R. A., et al. 2015, NatCo, 6, 7135
Panasenco, O., Martin, S. F., Velli, M., & Vourlidas, A. 2013, SoPh, 287, 391
Patsourakos, S., & Vourlidas, A. 2011, A&A, 525, A27
Raouafi, N. E., Patsourakos, S., Pariat, E., et al. 2016, SSRv, 201, 1
Sahade, A., Cécere, M., Costa, A., & Cremades, H. 2021, A&A, 652, A111
Sahade, A., Cécere, M., & Krause, G. 2020, ApJ, 896, 53
Sahade, A., Cécere, M., Sieyra, M. V., et al. 2022, A&A, 662, A113
Savage, S. L., McKenzie, D. E., Reeves, K. K., Forbes, T. G., & Longcope, D. W. 2010, ApJ, 722, 329
Scherrer, P. H., Bogart, R. S., Bush, R. I., et al. 1995, SoPh, 162, 129
Schrijver, C. J., & De Rosa, M. L. 2003, SoPh, 212, 165
Sieyra, M. V., Cécere, M., Cremades, H., et al. 2020, SoPh, 295, 126
Temmer, M., Preiss, S., & Veronig, A. M. 2009, SoPh, 256, 183
Thernisien, A., Vourlidas, A., & Howard, R. A. 2009, SoPh, 256, 111
Thompson, W. T., Kliem, B., & Török, T. 2012, SoPh, 276, 241
van Driel-Gesztelyi, L., & Green, L. M. 2015, LRSP, 12, 1
Vourlidas, A., Lynch, B. J., Howard, R. A., & Li, Y. 2013, SoPh, 284, 179
Wang, J., Hoeksema, J. T., & Liu, S. 2020, JGRA, 125, e27530
Wang, R., Liu, Y. D., Dai, X., et al. 2015, ApJ, 814, 80
Wyper, P. F., Antiochos, S. K., DeVore, C. R., et al. 2021, ApJ, 909, 54
Yang, J., Dai, J., Chen, H., Li, H., & Jiang, Y. 2018, ApJ, 862, 86
Zhang, J., Dere, K. P., Howard, R. A., Kundu, M. R., & White, S. M. 2001, ApJ, 559, 452
Zhang, Q. M. 2021, A&A, 653, L2
Zuccarello, F. P., Bemporad, A., Jacobs, C., et al. 2012, ApJ, 744, 66